Sub-10 second fly-scan nano-tomography using machine learning

Jiayong Zhang, Wah-Keat Lee, Mingyuan Ge*

National Synchrotron Light Source II (NSLS-II), Brookhaven National Laboratory, Upton, NY 11973, USA

Email: Mingyuan@bnl.gov

Supplementary Note 1: Derivation of Eq.2 in the main text

Definitions:

I_0 : integrated incident beam intensity within single exposure time t.

n : number of sub-angle intervals

I : integrated beam intensity after material absorption within single exposure time t.

I_i : beam intensity after material absorption at each angle interval, *i=1,2,…,n*

$\overline{I}$: averaged beam intensity after material absorption at each angle interval

$\mu = \mu(\theta, r)$: attenuation coefficient

$$I = \sum_{i=1}^{n} I_i = n\overline{I} \qquad \text{Eq. S1}$$

In this equation, we set the value of n to ensure that the blurring at the farthest distance from the image center is approximately 1 pixel. Thus, the blurring varies linearly from the edge of the image where the blurring is ~ 1 pixel, to the center of the image where the blurring will be << 1 pixel. Therefore, the variation of the measured projection image intensity I_i at each sub-angle interval (i) is very small. We can write the image intensity I_i respective to the average intensity $\bar{I}$ modified by a small variation Δ_i:

$$I_i = \bar{I}(1 + \Delta_i) \qquad \text{Eq. S2}$$

$$\Delta_i \rightarrow 0 \qquad \text{Eq. S3}$$

$$\sum_i^n \Delta_i = 0 \qquad \text{Eq. S4}$$

At each small angle interval:

$$I_i = \frac{I_0}{n} exp\left(-\int \mu_i dr\right) \qquad \text{Eq. S5}$$

$$\ln\left(\frac{nI_i}{I_0}\right) = -\int \mu_i dr \qquad \text{Eq. S6}$$

$$\because \sum_{i=1}^{n} \ln\left(\frac{nI_i}{I_0}\right) = \sum_{i=1}^{n} \ln\left(\frac{n\bar{I}}{I_0}(1+\Delta_i)\right) = \sum_{i=1}^{n}\left(\ln\left(\frac{I}{I_0}\right) + \ln(1+\Delta_i)\right) = n\ln\left(\frac{I}{I_0}\right) + \sum_{i=1}^{n}\ln(1+\Delta_i)$$

Eq. S7

$$\therefore -\ln\left(\frac{I}{I_0}\right) - \frac{1}{n}\sum_{i=1}^{n}\ln(1+\Delta_i) = \int\left(\frac{1}{n}\sum_{i=1}^{n}\mu_i\right)dr \qquad \text{Eq. S8}$$

$$\therefore -\ln\left(\frac{I}{I_0}\right) = \int\sum_{i=1}^{n}\mu_i dr + \frac{1}{n}\sum_{i=1}^{n}\Delta_i + \frac{1}{n}\sum_{i=1}^{n}\sum_{k=2}^{\infty}\frac{(-1)^{k-1}}{k}\Delta_i^k \qquad \text{Eq. S9}$$

$$\because \sum_{i=1}^{n}\Delta_i = 0 \qquad \text{Eq. S10}$$

$$\therefore -\ln\left(\frac{I}{I_0}\right) = \int\sum_{i=1}^{n}\mu_i dr + \frac{1}{n}\sum_{i=1}^{n}\sum_{k=2}^{\infty}\frac{(-1)^{k-1}}{k}\Delta_i^k \qquad \text{Eq. S11}$$

$$\therefore -\ln\left(\frac{I}{I_0}\right) = \int\left(\frac{1}{n}\sum_{i=1}^{n}\mu_i\right)dr + O(\Delta^2) + O(\Delta^3) + \cdots \qquad \text{Eq. S12}$$

$$\therefore -\ln\left(\frac{I}{I_0}\right) \approx \int\frac{1}{n}\sum_{i=1}^{n}\mu(\theta+(i-1)\delta\theta)\,dr \qquad \leftarrow\text{Eq. 2 in the main text}$$

Supplementary Note 2: Solving Eq. 7 in main text using ADMM[1]

Eq. 7 and Eq. 8 are copied from the main text:

$$\boldsymbol{\mu}^* = \underset{\boldsymbol{\mu}}{\operatorname{argmin}}\left(\frac{1}{2}\left\|\mathrm{y} - \widetilde{\mathbf{R}}\times\boldsymbol{\mu}\right\|_{\Omega}^{2} + \mathbf{D}\boldsymbol{\mu}\right) \quad \text{Eq. S13}$$

$$\Omega = diag\{y_i\} \quad \text{Eq. S14}$$

Eq. S13 can be formulated as:

$$\boldsymbol{\mu}^* = \underset{\boldsymbol{\mu}}{\operatorname{argmin}}\left(\frac{1}{2}\left\|\mathrm{y} - \widetilde{\mathbf{R}}\times\boldsymbol{\mu}\right\|_{\Omega}^{2} + \gamma|z|_1\right) \quad \text{Eq. S14}$$

$$s.t \quad z = \mathbf{D}\boldsymbol{\mu} \qquad \text{Eq. S15}$$

The augmented Lagrangian for this problem is given by:

$$L(\mu, z, u) = \frac{1}{2}\left\|\mathrm{y} - \widetilde{\mathbf{R}}\times\boldsymbol{\mu}\right\|_{\Omega}^{2} + \rho u^{\mathrm{T}}(\mathbf{D}\boldsymbol{\mu} - \mathrm{z}) + \frac{\rho}{2}\|\mathbf{D}\boldsymbol{\mu} - \mathrm{z}\|_{\Omega}^{2} \qquad \text{Eq. S16}$$

μ, z, u can be iteratively updated by:

$$\boldsymbol{\mu}^* = \underset{\boldsymbol{\mu}}{\operatorname{argmin}}\big(L(\mu, z, u)\big)$$

$$\mathbf{z}^* = \underset{\mathbf{z}}{\operatorname{argmin}}\big(L(\mu, z, u)\big)$$

$$u^{*} = u + (\mathbf{D}\boldsymbol{\mu} - \mathrm{z})$$

Supplementary Note 3: Training dataset preparation

Our dataset consists of 1600 images (512x512 pixels) from the four categories, as shown in **Figure 2** in the main text. All images have been normalized to [0, 1]. We split the dataset by the ratio of 9:1 for training and validation purposes. We argue that even though the dataset is designed for this experiment, one can easily design and custom a training dataset to better suit a specific need. For example, one may design a dataset containing lungs with prior known experimentally observed patterns to be applied in medical imaging of lungs. The training data shown in Figure 2c-e are generated with the assistance of using the *PoreSpy* package[2].

Supplementary Note 4: Evaluation of ML reconstruction on varied image conditions

To evaluate the mode performance, we averaged the results from 50 simulated images at each combination of noise level (in terms of Poisson noise generated from various incident beam intensities) and the different number of projection images (corresponding to different sample rotation speeds). Comparing the ML and FBP methods, we found significant improvements in both PSNR and SSIM. **Fig. S1** shows the results.

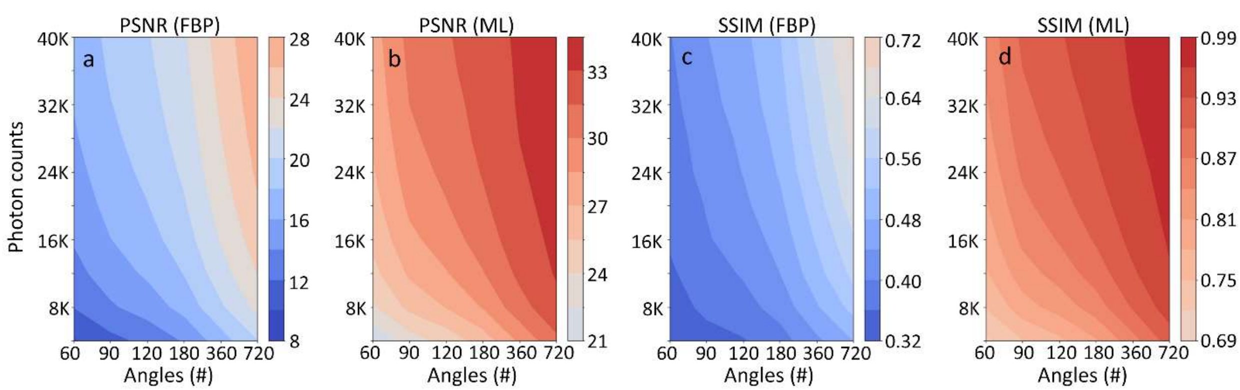

Fig. S1 (a) PSNR of FBP reconstruction averaged from 50 test cases at each combination of projection numbers and photon counts. **(b)** PSNR of ML reconstruction. **(c)** SSIM of FBP reconstruction. **(d)** SSIM of ML reconstruction. Note that, small photon counts indicate large noise. A small angle-number corresponds to fast rotation speed.

In **Fig. S2**, we compare the ML performance under three different imaging conditions. We assume 0.05 sec exposure time for individual projection image and a constant camera frame rate of 20 frames per second.

Rotation speeds at 30 deg/sec, 60 deg/sec and 120 deg/sec lead to a collection of 120, 60 and 30 projection images in the fly-scan. No significant performance degradation is found in the reconstructions from 120 and 60 projections (**Fig. S2e** and **2f**). Further reducing the number of projections to 30 (by increasing the speed to 120 deg/sec) gives few reconstruction artifacts as manifested in the red square regions, which display some small holes as showing in **Fig. S2g**. This kind of hole artifacts originate from the noisy FBP reconstruction in **Fig. S2d**. Indicated by the red arrows in **Fig. S2d**, the ML fausely interprete the low counts region as a hole.

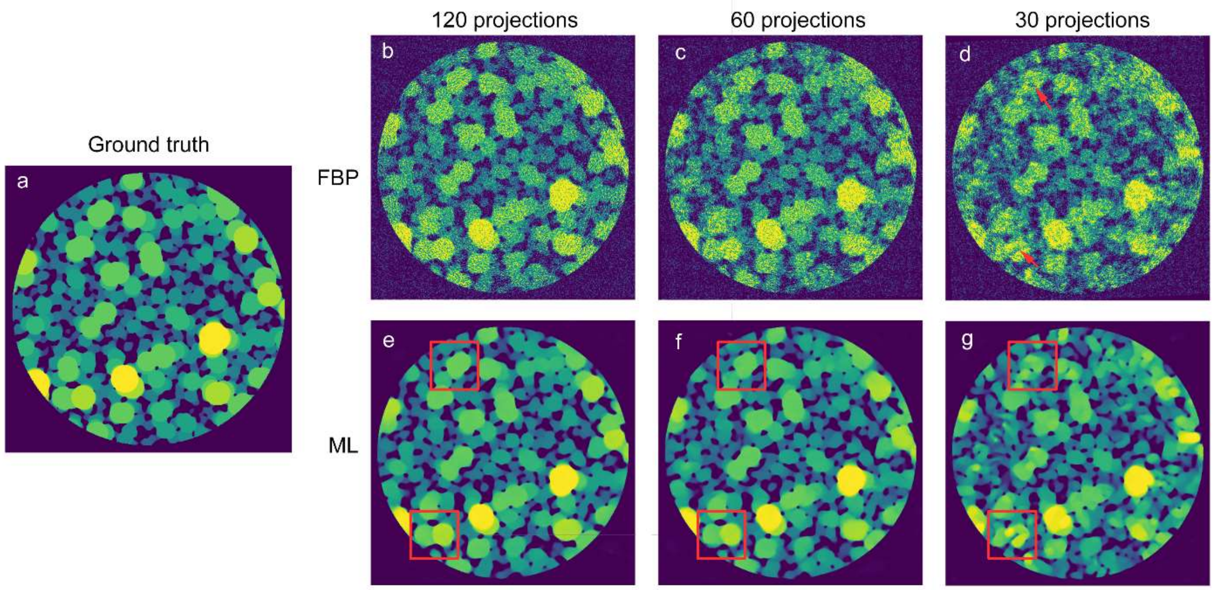

Fig. S2 Comparison of ML reconstruction for simulated fly-scan at different rotation speeds. (a) ground truth image. **(b-d)** FBP reconstruction. **(e-g)** ML reconstruction. Specifically, **(b, e)** fly-scan at rotation speed of 30 deg/sec, corresponding to a collection of 120 projection images assuming the expeosure time of 0.05sec for each projection. **(c, f)** fly-scan at rotation speed of 60 deg/sec, corresponding to a collection of 60 projection images. **(d, g)** fly-scan at rotation speed of 120 deg/sec, corresponding to a collection of 30 projection images.

We also test the ML performance on a different type of images with polygon geometries. Imaging conditions are the same as before. **Fig. S3e-g** present the ML results. Similarly, at rotation at 30 deg/sec (120 projections) and 60 deg/sec (60 projections), ML gives similar reconstruction quality. However, performance degrades at fast ration condition (**Fig. S3g**, 120 deg/s, 30 projections). It is noted that ML can preserve the sharp edge boundaries, but with slight blurring on the corner (see the enlarged view in **Fig. S3e1**). This is because the ML is mostly trained on smooth objects as presented in the **Fig. 2d-g** in the main text. We can remedy this blurring issue by further training the ML using geometries with sharp boundaries and corners. As shown in **Fig. S3h-j** and **Fig. S3h1**, those sharp features can be well reconstructed.

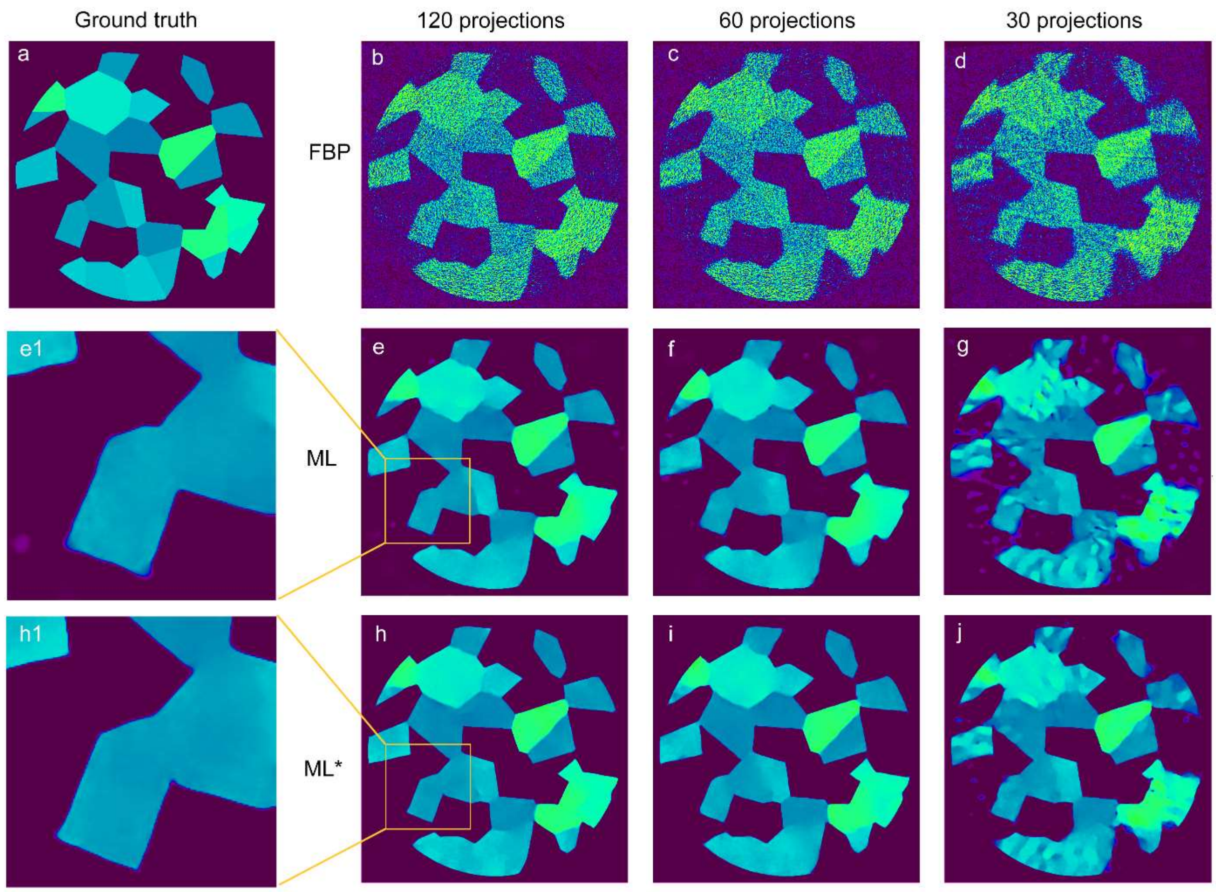

Fig. S3 Comparison of ML reconstruction on polygon shapes in the simulated fly-scan at different rotation speeds. (a) ground truth image. **(b-d)** FBP reconstruction. Specifically. **(e-g)** ML reconstruction. **(h-j)** results from ML with additional training on polygon shaped geometric images. Specifically, **(b, e, h)** fly-scan at rotation speed of 30 deg/sec, corresponding to a collection of 120 projection images assuming the expeosure time of 0.05sec for each projection. **(c, f, i)** fly-scan at rotation speed of 60 deg/sec, corresponding to a collection of 60 projection images. **(d, g, j)** fly-scan at rotation speed of 120 deg/sec, corresponding to a collection of 30 projection images. **(e1)** and **(h1)** are the enlarged view of the square regions indicated in **(e)** and **(h)** respectively.

Supplementary Note 5: In-situ heating experiment

5.1 Tomography data collection

The TXM experiment is carried out at the FXI beamline at NSLS-II at Brookhaven National Laboratory. FXI is equipped with a Fresnel Zone plate with 30nm outmost zone width as the objective lens. The translation xyz sample stage and the rotary stage are equipped with encoders. The rotation stage has a negligible round-out error[3] and so, the xyz sample stage on top of the rotary stage is not used to correct run-out errors, as is often done in set-ups where the rotation stage has large run-out errors. It is also noted that, the rotation angles are directly read from the time-stamped absolute encoder as 32-bit floating numbers. The effective pixel size recorded in the CCD camera is 40 nm. We estimate the actual 3D spatial resolution to be < 50nm in this instrument[4].

Data was collected by fly-scans during the experiment. The sample was continuously rotating from 0-900 degrees at a rotation speed of 15 deg/sec. The camera was set in the 'free-run' mode and its frame rate is ~ 20-25 frames per second. The frame rate can vary a bit during data acquisition to data transfer and network traffic. Each acquired image is saved along with a time-stamp. Exposure time is 0.04 sec for each individual projection image, and in total, ~ 1500 projection images were collected for the 900 degree scan. We then took the dark image (without X-ray) and flat-field image (without sample), which introduces some time overhead before starting the next fly-scan (rotate from 900-0 degrees). For each 900-degree scan, we divide the ~ 1500 images into five groups. Each image group covering a rotation range of 180 degrees was used to reconstruct the 3D structure. Because the images are collected in the 'free-run' camera mode, they may not be separated by equal time (or angle) intervals. Thus, before reconstruction, each image is assigned an angle based on the interpolation of the time-stamped encoder readings. In reconstruction, we also used the off-the-shelf algorithm[6] to reduce any ring artifacts.

5.2 Crack extraction

We use the output from ML to extract the volume fraction of cracks, as presented in Fig 5. Specifically, we use Gaussian blurring to blur the image, and the blurring will effectively fill the cracks. We count the number of pixels with a value larger than 0 to get the volume of the particle. Within the particle (output from ML), voxel values smaller than 5% of the mean value (in the particle) are treated as cracks. The volume fraction is calculated as the ratio of (number of crack voxels) / (volume of the particle).

5.3 Crack visualization

Supplementary Fig. S4 shows a slice view of reconstruction at different heating states. Those images with red dots correspond to the images we presented in the main text. For comparison, **Supplementary Fig. S5** displays the outputs from the ML model.

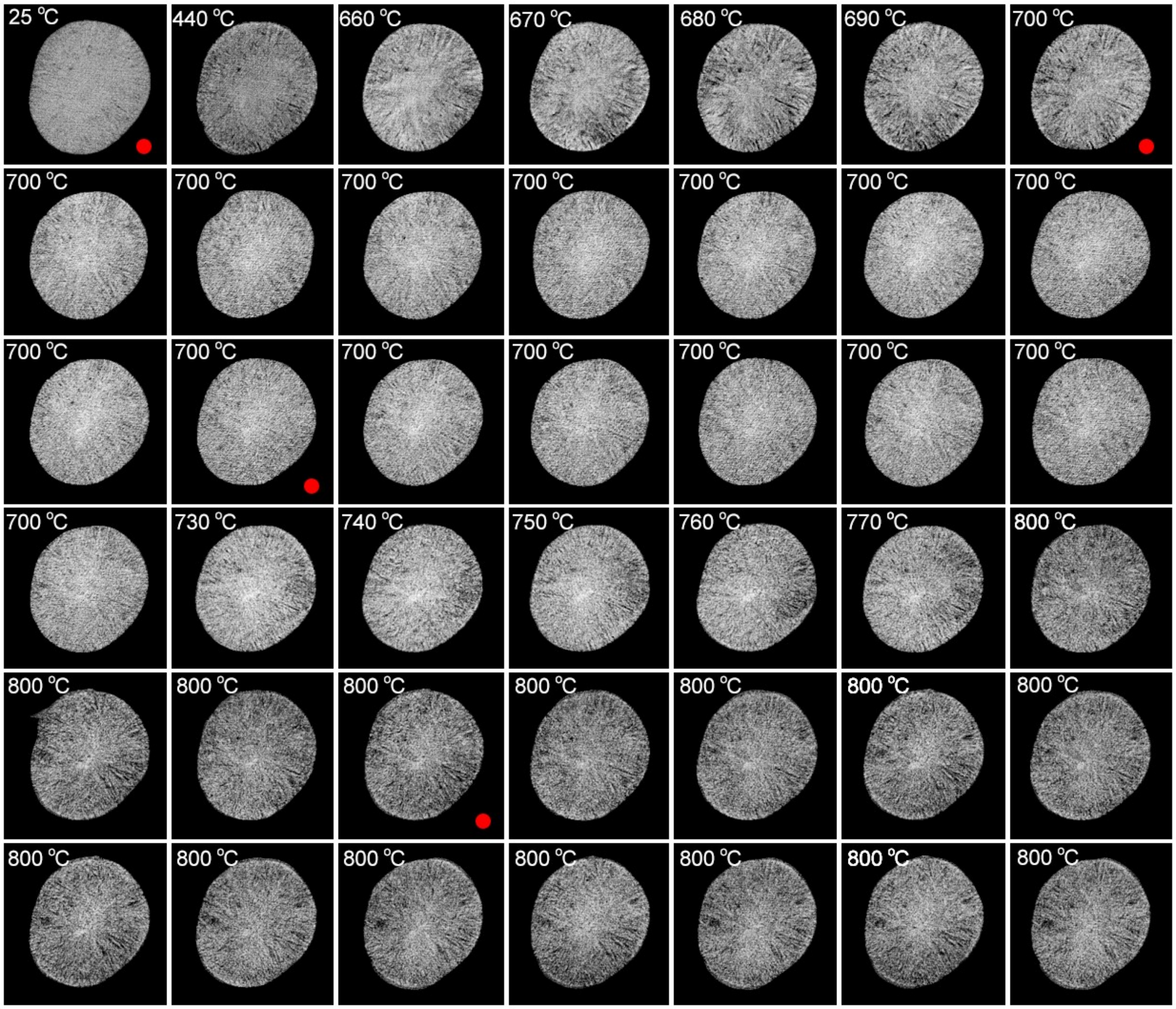

Fig. S4. A slice view of tomography reconstruction of the particle during in-situ heating experiments. The images with red dots correspond to the images presented in Figure 5 in the main text.

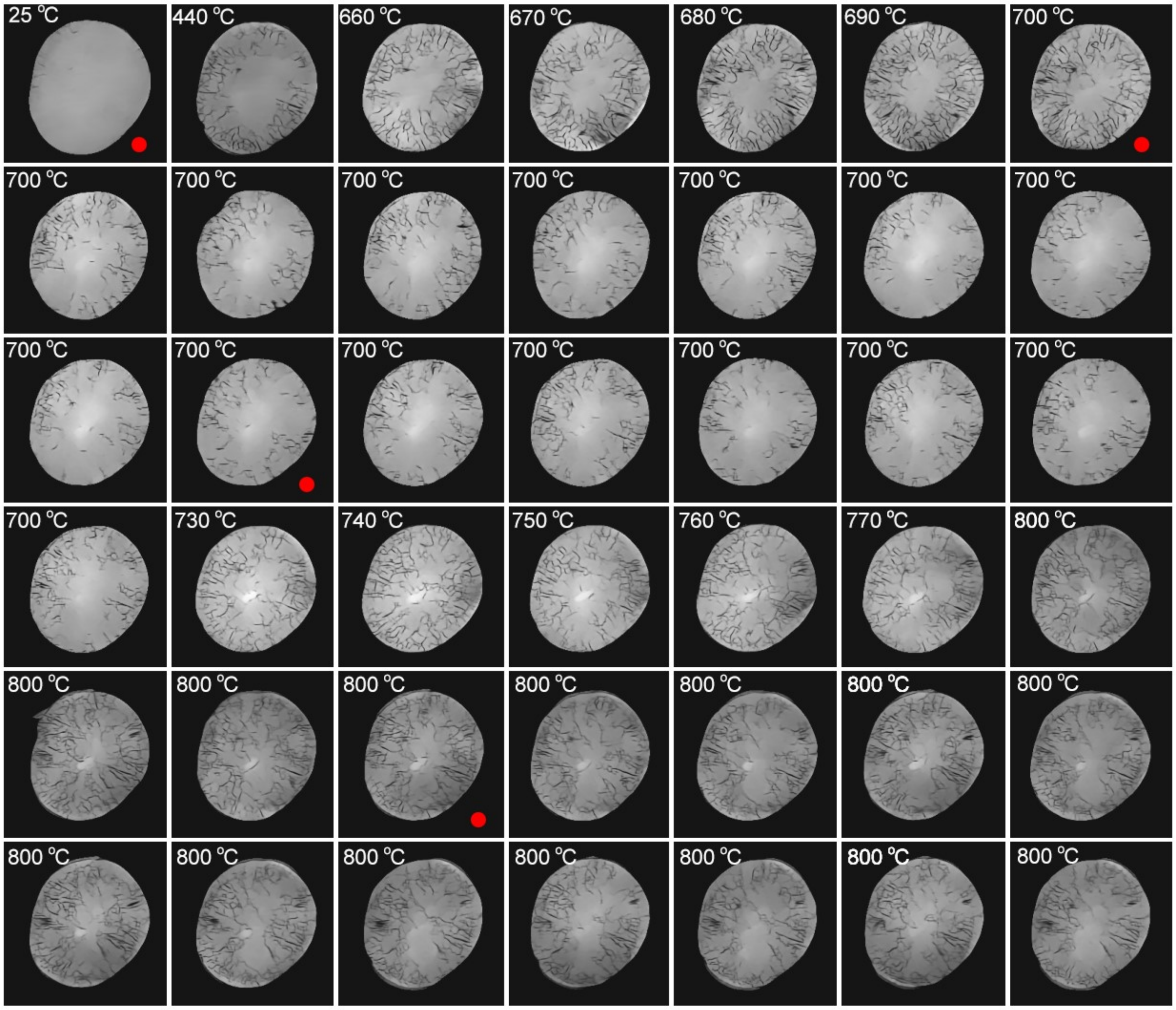

Fig. S5. A slice view from the output of the machine learning model.

Supplementary References:

1. Boyd, S. P., *Distributed optimization and statistical learning via the alternating direction method of multipliers*. Now Publishers Inc.: Hanover, MA, 2011; p 126 p.
2. J. T. Gostick, Z. A. K., T. G. Tranter, M. D. r Kok, M. Agnaou, M. Sadeghi, R. Jervis, PoreSpy: A Python Toolkit for Quantitative Analysis of Porous Media Images. *Journal of Open Source Software* **4**, 4 (2019).
3. Coburn, D. S., et al., Design, characterization, and performance of a hard x-ray transmission microscope at the National Synchrotron Light Source II 18-ID beamline. *Rev Sci Instrum* **90**, (2019).
4. Ge, M. Y., et al., One-minute nano-tomography using hard X-ray full-field transmission microscope. *Appl Phys Lett* **113**, (2018).